

# Environmental Science Atmospheres

Accepted Manuscript

This article can be cited before page numbers have been issued, to do this please use: Y. S. HAM, H. S. Ri, K. Sonu, S. Jong and U. S. Paek, *Environ. Sci.: Atmos.*, 2026, DOI: 10.1039/D6EA00029K.



This is an Accepted Manuscript, which has been through the Royal Society of Chemistry peer review process and has been accepted for publication.

Accepted Manuscripts are published online shortly after acceptance, before technical editing, formatting and proof reading. Using this free service, authors can make their results available to the community, in citable form, before we publish the edited article. We will replace this Accepted Manuscript with the edited and formatted Advance Article as soon as it is available.

You can find more information about Accepted Manuscripts in the [Information for Authors](#).

Please note that technical editing may introduce minor changes to the text and/or graphics, which may alter content. The journal's standard [Terms & Conditions](#) and the [Ethical guidelines](#) still apply. In no event shall the Royal Society of Chemistry be held responsible for any errors or omissions in this Accepted Manuscript or any consequences arising from the use of any information it contains.

This study advances atmospheric science by developing a machine learning framework for 1-year-lead summer rainfall prediction over the northern Korean Peninsula, a data-sparse region highly vulnerable to climate variability. By introducing regionally optimized spatial-contrast indices that capture large-scale circulation gradients between Siberia and eastern China, the work enhances understanding of mid-latitude atmospheric drivers of regional precipitation. The approach addresses critical gaps in long-lead forecasting for Northeast Asia, supporting climate adaptation in agriculture, water resources, and disaster risk management. Methodologically, integrating spatial pattern analysis with neural networks offers a transferable strategy for improving seasonal prediction in observation-limited regions, contributing to global environmental risk assessment and resilience planning under a changing climate.

View Article Online  
DOI:10.1039/D6EA00029K



# Machine learning-based 1-year-lead summer precipitation prediction over the DPRK using regionally optimized spatial-contrast indices

View Article Online

DOI: 10.1039/D6EA00029K

Yong-Sik Ham<sup>1,2\*</sup>, Hyon Su Ri<sup>1</sup>, Kyong-Bok Sonu<sup>1,2</sup>, Sang-Il Jong<sup>1</sup>, Un Sim Paek<sup>1</sup>

<sup>1</sup> *Department of Meteorology, Faculty of Global Environmental Science, Kim Il Sung University, Pyongyang, DPR Korea*

<sup>2</sup> *School of Water Resources and Environmental Science, China University of Geosciences (Beijing)*

*First Author address(Corresponding): Yong-Sik Ham: E-mail: [hys12211126@163.com](mailto:hys12211126@163.com)*

*Author address: Hyon-Su Ri, E-mail: [wanglong\\_animation@163.com](mailto:wanglong_animation@163.com)*

*Author address: Kyong-Bok Sonu: [sukb0819@163.com](mailto:sukb0819@163.com)*

*Author address: Sang-Il Jong, E-mail: [horangyi11@163.com](mailto:horangyi11@163.com)*

*Author address: Un-Sim Paek, E-mail: [pus19920427@163.com](mailto:pus19920427@163.com)*

## ABSTRACT

The northern part of the Korean Peninsula (NPKP) is a region highly dependent on summer monsoon precipitation for water resources and disaster risk management, and reliable one-year-ahead prediction of summer precipitation is pivotal for formulating climate adaptation strategies. Using the NCEP/NCAR reanalysis dataset spanning 75 years (1948–2022) and precipitation data from 37 meteorological stations in the Democratic People's Republic of Korea, this study developed regionally optimized spatial-contrast indices to explain the interannual variability of summer precipitation. The results show that the circulation patterns with high concurrent correlation with summer precipitation do not persist into the following year. However, the deepened low-pressure system over inland Eurasia, particularly around Lake Baikal, in the preceding summer ( $t-1$ ) exhibits a significant lagged correlation with summer precipitation ( $t$ ). Based on this physical insight, the study designed spatial-contrast indices that quantify the regional circulation anomaly differences between Siberia and eastern China. A back-propagation neural network (BPNN) trained on these indices achieved an anomaly correlation coefficient (ACC) of 0.59, a root mean square error (RMSE) of 134.61 mm, and a mean bias error (MBE) of  $-4.22$  mm during the 5-fold cross-validation period (1949–2022), significantly outperforming traditional linear regression models. These findings demonstrate that regionally optimized atmospheric circulation indices provide robust predictive skill for long-lead precipitation forecasting in data-scarce regions.



36 **Key words:** East Asian summer monsoon (EASM) · Western Pacific subtropical high (WPSH) ·  
37 Northern East Asian low (NEAL) · Atmospheric circulation index · Back-propagation neural  
38 network (BPNN), Summer precipitation

## 40 1. Introduction

41 Reliable long lead forecasting of summer precipitation is a cornerstone of climate resilience in  
42 monsoon dependent societies. Over the northern part of the Korean Peninsula (NPKP), where water  
43 security hinges on a narrow seasonal window, summer precipitation delivers more than half of the  
44 annual total.<sup>1,2</sup> Yet this concentration also renders the region acutely vulnerable: intense  
45 precipitation episodes, often amplified by typhoon interactions or stalled frontal systems, can trigger  
46 flash floods and landslides, disrupting food systems, infrastructure, and human safety. Conversely, a  
47 weak Jangma (Meiyu/Baiu) season may precipitate agricultural drought within weeks. In this  
48 context, annual lead prediction, issued before the onset of the preceding winter, holds exceptional  
49 operational value, enabling early allocation of reservoir capacity, crop planning, and disaster  
50 preparedness.

51 The Jangma front, recognized as the regional manifestation of the East Asian summer  
52 monsoon (EASM) over the Korean Peninsula, lies climatologically between the Meiyu (China) and  
53 Baiu (Japan) subsystems <sup>3., 4., 5.</sup> Unlike idealized monsoons driven by land–sea thermal contrast,  
54 Jangma is maintained through a delicate convergence of four distinct airmass sources: (i) warm,  
55 moist inflow from the South China Sea; (ii) dry, cool outflow from the Siberian high; (iii) subsiding  
56 air under the western Pacific subtropical high (WPSH); and (iv) cold, moist advection from the  
57 Okhotsk Sea <sup>6., 7., 8., 9.</sup>

58 Crucially, the intensity and persistence of these moisture-laden flows are influenced not only  
59 by atmospheric circulation but also by slowly varying boundary forcings such as oceanic or  
60 land-surface conditions in some monsoon systems <sup>10., 11., 12., 13.</sup> While oceanic precursors  
61 including mixed-layer temperature and mean sea level anomalies exhibit high skill for Indian  
62 monsoon precipitation forecasting, their utility diminishes over the northern East Asian monsoon  
63 domain due to the increasing dominance of mid-latitude dynamics <sup>14., 15., 16.</sup>

64 ENSO, though a leading driver of tropical–subtropical monsoon variability on interannual  
65 timescales, exerts a highly modulated influence over the Korean Peninsula. Its teleconnection is  
66 nonlinear, contingent not only on ENSO’s spatial flavor but also on the background state of the  
67 extratropical circulation <sup>17.</sup> As <sup>18.</sup> emphasized, skillful prediction of the East Asian summer  
68 monsoon requires explicit representation of mid-latitude precursors such as Eurasian snow cover or  
69 the Silk Road pattern that can override or amplify remote ENSO signals depending on their phase  
70 and evolution. Consequently, even remotely forced SST anomalies that enhance predictability in the



71 Indian or southern East Asian sectors [13](#). are strongly attenuated by the time they reach the NPKP,  
72 where local atmospheric configurations, particularly the Baikal-centered low and the extended  
73 Northern East Asian low (NEAL), emerge as the dominant indicators of interannual predictability  
74 linked to boundary memory.

75 This diagnostic gap motivates a shift from global index local response paradigms toward  
76 regionally tailored predictor design. A growing body of work suggests that predictive skill at  
77 multi-month to annual leads may reside not in the magnitude of individual anomalies, but in their  
78 spatial configuration; for example, zonal asymmetries in the WPSH, meridional shear across the  
79 mid-latitude jet, or dipole structures in Eurasian surface pressure [19.](#), [20.](#), [21](#). Notably, [22](#). identified  
80 NEAL as a cyclonic feature whose persistence modulates moisture transport into the NPKP.  
81 However, its predictive utility remains underexplored, particularly in lagged contexts. Moreover,  
82 cyclone tracks originating from the Huai River basin, a key moisture conduit, show marked decadal  
83 shifts that are poorly represented by coarse-scale indices. These observations point to a critical  
84 need: to develop circulation metrics that encode dynamic gradients, not just area means.

85 From a methodological standpoint, the choice of modeling framework must align with both the  
86 nonlinear nature of monsoon precipitation and the operational demand for skill, robustness, and  
87 interpretability. While linear regression remains a standard benchmark, as demonstrated by [23.](#), who  
88 achieved significant skill in forecasting East Asian summer monsoon precipitation using oceanic  
89 heat sources in a multiple linear regression framework, its performance degrades markedly in the  
90 presence of threshold effects, regime shifts, and tail events, which are intrinsic to Korean Peninsula  
91 hydroclimate [24.](#), [25](#). In contrast, artificial neural networks, particularly the back-propagation neural  
92 network (BPNN), require no prespecified functional form and can approximate arbitrarily complex,  
93 nonlinear input–output mappings [26.](#), [27](#). Recent studies confirm their superiority in capturing  
94 high-magnitude precipitation events, where linear models systematically underperform [21.](#), [28](#).  
95 Though neuro-fuzzy systems show promise [28.](#), BPNN retains advantages in training stability,  
96 scalability, and sensitivity to extreme quantiles [13.](#), qualities that are essential for operational  
97 forecasting of flood- and drought-triggering precipitation over the NPKP. Notably, even in  
98 mid-latitude settings where dynamical memory is weak, purely statistical approaches remain  
99 competitive: [29](#). showed that a simple linear model using North Atlantic precursors achieved skill  
100 comparable to state-of-the-art dynamical ensembles in predicting winter wind speeds over China.  
101 This supports our strategy of prioritizing regionally optimized statistical predictors over global  
102 dynamical outputs, particularly when long-lead skill is sought in data-scarce regions [30.](#), [19.](#), [31](#).

103 Accordingly, this study aims to develop a reliable annual lead forecasting framework for  
104 summer precipitation over the northern part of the Korean Peninsula (SR-NPKP). To this end, we  
105 focus on three core objectives. First, we will investigate the interannual variabilities of SR-NPKP,



106 WPSH index (WPSHI), and NEAL index (NEALI). Second, we will analyze the simultaneous and  
107 one-year-lagged correlations between large-scale circulation patterns and SR-NPKP and explore the  
108 underlying physical mechanisms. Third, we will assess the performance of one-year-ahead  
109 prediction experiments for SR-NPKP. This assessment will involve a comparative evaluation of  
110 multiple model classes, including BPNN and standard linear regression models. The goal is to  
111 rigorously benchmark their forecast skill for both mean conditions and extreme precipitation  
112 quantiles.

113 The remainder of this paper is structured as follows. Section 2 details the data sources and  
114 methodology employed. In Section 3, we present the results. We begin by examining the observed  
115 variabilities of the key indices. Then, we analyze the diagnostic relationships and plausible  
116 mechanisms linking circulation patterns to SR-NPKP. Finally, we evaluate and discuss the  
117 comparative skill of the 1-year-lead prediction experiments using BPNN and linear models. The  
118 paper concludes with a summary and discussion of the main findings in Section 4.

## 120 2. Data and methodology

### 121 2.1. Data and Study Area

122 This study employs two complementary datasets to investigate the long-lead predictability of  
123 summer (June–August) precipitation over the NPKP. The spatial domain of the study region and the  
124 station distribution are shown in Fig. 1.

125 For the analysis of large-scale atmospheric circulation, monthly mean fields from the  
126 NCEP/NCAR Reanalysis I dataset [32](#) are used. The analysis covers the 75-year period from 1948  
127 to 2022 and is restricted to the boreal summer season. The following variables were extracted: sea  
128 level pressure (SLP), geopotential height at 500 hPa, and zonal wind ( $u$ ), meridional wind ( $v$ ), and  
129 air temperature ( $T$ ) at four standard pressure levels (1000, 850, 700, and 500 hPa). All reanalysis  
130 data are provided on a  $2.5^\circ \times 2.5^\circ$  horizontal grid. The vertical resolution was intentionally limited  
131 to these levels to ensure robustness in the lead–lag correlation analysis and to mitigate the risk of  
132 overfitting during predictor selection.

133 For forecast verification, observed summer precipitation data were obtained from the State  
134 Hydro-Meteorological Administration (SHMA) of the Democratic People’s Republic of Korea. An  
135 initial pool of 183 stations was screened for temporal completeness and internal consistency. A final  
136 network of 37 stations was retained, each possessing uninterrupted June–August precipitation  
137 records spanning the full 75-year period (1948–2022). Prior to data release, the SHMA applied  
138 standardized quality assurance procedures, including inter-station consistency checks,  
139 homogenization for instrument and observing practice changes, and correction for wind-induced  
140 undercatch. The final dataset was further subjected to independent verification using breakpoint



141 detection and inter-station coherence analysis, with no major unresolved inconsistencies identified.



Fig 1. The spatial domain of the study region and the station distribution

## 2.2. Methodology

This study aims to establish a 1-year lead prediction system for SR-NPKP. To this end, the atmospheric circulation field was quantified using two key indices:

WPSHI: average of 500 hPa geopotential height anomalies over 20°–25°N, 125°–140°E [33.](#), [8.](#)

NEALI:  $-1 \times$  (average of 850 hPa geopotential height anomalies over 45°–60°N, 110°–130°E)

[22.](#) The negative sign ensures that higher NEALI values correspond to stronger cyclonic activity (lower geopotential height).

A linear least squares fit was applied to the 1948–2022 time series of SR-NPKP, WPSHI, and NEALI to remove the long-term linear trend. Subsequent analyses (e.g., correlation, predictor construction) were performed only on the detrended interannual components to isolate year-to-year variability from secular trends. A 21-year moving mean [34.](#) was computed for SR-NPKP to isolate low-frequency fluctuations. Abrupt shifts were detected using the Mann–Kendall nonparametric test [35.](#), [36.](#), a rank-based method robust to non-normality; a statistically significant change point is identified when the forward (UF) and backward (UB) cumulative rank statistics intersect above the 95% confidence envelope.

To identify predictors for 1-year lead forecasting, pointwise Pearson correlations were calculated between SR-NPKP in year  $t$  and summer (June–August) anomalies of sea level pressure



162 (SLP), geopotential height, air temperature (T), zonal (u), and meridional (v) wind at 1000, 850,  
163 700, and 500 hPa from the NCEP/NCAR Reanalysis I 32. over 10°–70°N in the preceding year (1949–  
164 1). Only detrended interannual components were used. The 1-year lead correlation thus corresponds  
165 to the relationship between atmospheric variables for 1948–2021 and SR-NPKP for 1949–2022.

166 Based on these maps, an area-shift experiment 37. was conducted, shifting the analysis domain  
167 in 2.5° increments to compute regional averages. Spatial-contrast indices—primarily differences  
168 (and select linear combinations) of anomalies between dynamically linked subregions (NEAL core  
169 vs. WPSH edge)—were constructed to enhance physical interpretability and reduce redundancy.  
170 Though historically termed “spatial-contrast indices”, the selected indices predominantly represent  
171 zonal/meridional gradients or dipole structures, consistent with evidence that spatial configuration  
172 often outperforms single-area means in seasonal prediction 19., 20., 21.

173 Only spatial-contrast indices whose Pearson correlation coefficients with SR-NPKP satisfy  $|r|$   
174  $\geq 0.4$  ( $p < 0.001$ ,  $n = 74$ ) were retained as candidate predictors. Here, the abbreviations denote:  
175 SLPA (sea level pressure anomaly), GPHA (geopotential height anomaly), TA (temperature  
176 anomaly), UA (zonal wind anomaly), and VA (meridional wind anomaly); numerical suffixes  
177 indicate pressure level (GPHA850) and analysis domain.

178 A backpropagation neural network (BPNN) was employed as the prediction model. As a  
179 feedforward neural network trained via gradient descent to minimize prediction errors 26., 27.,  
180 BPNN requires no predefined functional relationship and thus performs well in capturing the strong  
181 nonlinearity and threshold sensitivity characteristic of monsoon precipitation systems 38. The  
182 network architecture was structured as follows: the input layer consisted of the selected  
183 spatial-contrast indices; three hidden layers were adopted, each containing 10 neurons with a  
184 sigmoid activation function; and the output layer contained a single neuron representing the  
185 predicted summer rainfall over the DPRK (SR-NPKP).

186 In this study, the full dataset covering 1949–2022 was used for model development. To avoid  
187 overfitting and ensure the stability and reliability of model performance, 5-fold cross-validation was  
188 applied to the entire dataset. In this procedure, the full dataset was randomly divided into five  
189 subsets of equal size. In each fold, four subsets were used for training and the remaining one for  
190 validation; this process was repeated five times to determine the optimal model parameters.

191 Predictive performance was evaluated based on the results of 5-fold cross-validation. Three  
192 metrics were employed to comprehensively quantify forecast skill: the anomaly correlation  
193 coefficient (ACC) to assess anomaly prediction skill, root mean square error (RMSE) to quantify  
194 the overall magnitude of prediction errors, and mean bias error (MBE) to evaluate systematic over-  
195 or under-prediction..

196



### 197 3. Results and discussion

#### 198 3.1. Variabilities of SR-NPKP, and WPSH & NEAL intensities

View Article Online  
DOI: 10.1039/D6EA00029K

199

200 We investigated the annual variability and abrupt change characteristics of SR-NPKP, WPSHI and the  
201 NEALI over the period 1948–2022.

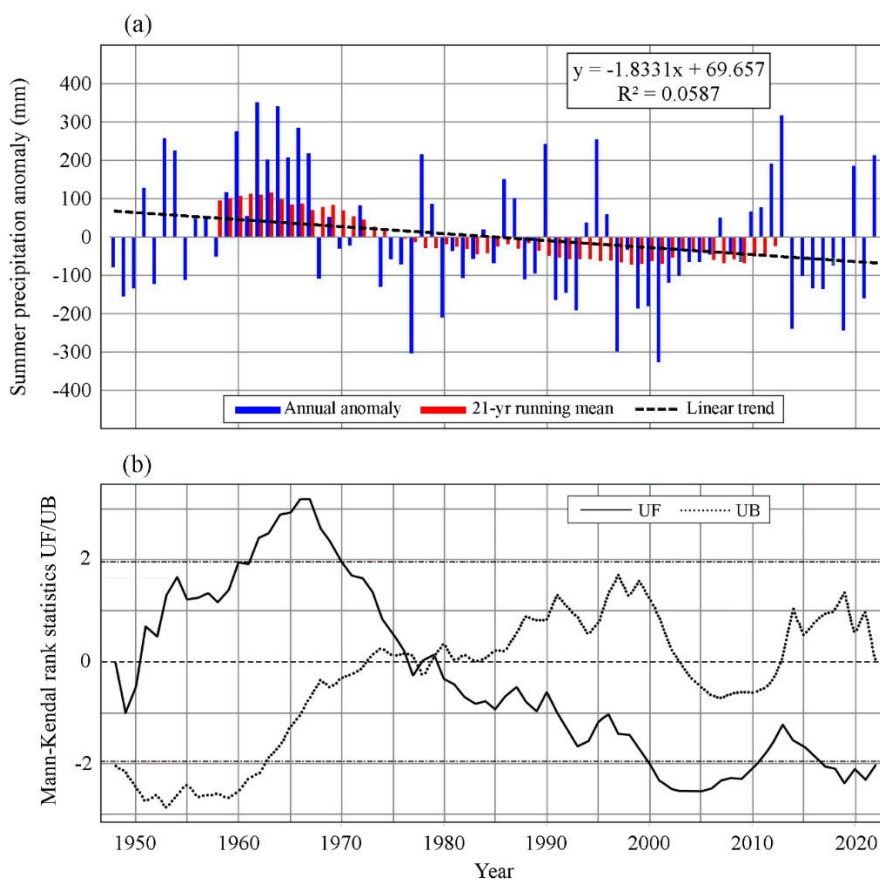
202 Anomalies of SR-NPKP (deviations from the long-term mean of 633.5 mm) show strong interannual  
203 variability, with a standard deviation of 164.9 mm — accounting for 26% of the mean. The 75-year  
204 SR-NPKP time series has a statistically significant linear decreasing trend ( $p = 0.03621$ ), with a decrease rate  
205 of 18.3 mm per decade (Fig. 2a). As a result of spectral analysis [39.](#), the three most prominent periodicities  
206 were found to be 8.3 years, 2.8 years, and 15.0 years.

207 The 21-year moving average (1958–2012) shows a distinct regime shift around the mid-1970s  
208 (Fig. 2a). Over the 27 years from 1948 to 1974, positive anomalies accounted for 16 years (59%)  
209 and negative anomalies for 11 years (41%), with above-average precipitation persisting overall, and  
210 there were no extreme drought years with anomalies less than  $-200$  mm. In contrast, over the 48  
211 years from 1975 to 2022, negative anomalies dominated at 32 years (67%), and extreme  
212 precipitation events exceeding  $+200$  mm (5 years) and less than  $-200$  mm (6 years) occurred with  
213 similar frequencies. This suggests that amid the overall decreasing trend, climate change has  
214 increased the variability of SR-NPKP, leading to more frequent extreme events such as droughts  
215 and floods.

216

217





View Article Online  
DOI: 10.1039/D6EA00029K

Fig. 2. The variability (a) and abrupt change (b) in SR-NPKP anomaly time series for the period of 1948–2022

The Mann–Kendall test was applied for statistical significance verification. The intersection of the forward statistic (UF) and backward statistic (UB) was confirmed within the 95% confidence interval in the mid-to-late 1970s, indicating that the abrupt shift in SR-NPKP is statistically significant. This result is consistent with the two regimes (1948–1974 and 1975–2022) derived from the moving average analysis, with the transition around 1974–1975.

Fig. 3a shows the long-term variation trend of the WPSHI. The long-term average value of the WPSHI is 5872.5 gpm, with a standard deviation of 11.1 gpm. It showed a significant increasing trend of +3.5 gpm per decade ( $p < 0.001$ ) over the entire period, and the intensity regime changed starting in the late 1970s. Over the 30 years from 1949 to 1978, negative anomalies were overwhelmingly prevalent at 28 years (93%), but over the 44 years from 1979 to 2022, positive anomalies shifted to dominate at 31 years (70%), and strong negative anomalies of  $-10$  gpm or less rarely occurred. Mann–Kendall test results showed that the abrupt change in WPSH intensity was statistically significant at the 95% or higher confidence level after 1986.

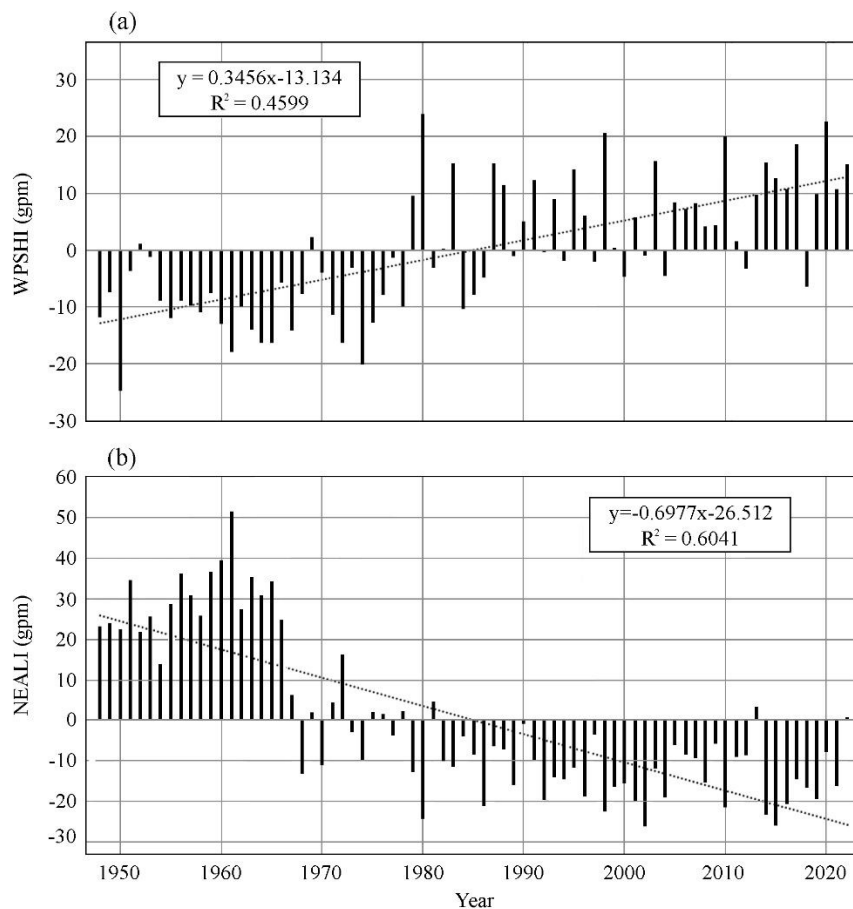
The NEALI exhibits a long-term mean of 1424.6 gpm and a standard deviation of 19.6 gpm (Fig. 3b). The time series exhibited a highly significant decreasing trend of  $-6.98$  gpm per decade ( $p < 10^{-15}$ ). Additionally, an abrupt regime shift occurred around 1974, transitioning from a positive phase (strong low pressure) to a negative phase (weak low pressure), which was also significant at



238 the 95% or higher confidence level.

239

View Article Online  
DOI: 10.1039/D6EA00029K



240

241

242

243

244

245

246

247

248

249

250

251

252

253

254

255

256

Fig. 3. The interannual variabilities of (a) WPSHI and (b) NEALI time series for 1948–2022. Dotted lines indicate the linear trends of WPSHI and NEALI time series for the study period

Simultaneous correlation analysis results showed that the correlation coefficient between WPSHI and SR-NPKP was  $-0.18$  ( $p > 0.05$ ), which is not statistically significant. This indicates that the interannual variability of Western Pacific Subtropical High intensity does not exhibit a direct and stable linear relationship with SR-NPKP. In contrast, the correlation coefficient between NEALI and SR-NPKP was  $+0.47$  ( $p < 0.001$ ), demonstrating a robust concurrent relationship: stronger Northeast Asian low pressure activity (i.e., decreased geopotential height anomalies  $\rightarrow$  increased NEALI) is associated with greater summer precipitation in the same year. This result aligns with the physical mechanism proposed by 22., which holds that the interannual variability of East Asian summer precipitation is primarily regulated by the activity of mid-latitude low pressure systems in Northeast Asia.

However, for 1-year lead forecasting, lag-1 correlation (1-year delayed correlation) is more critical than simultaneous correlation. As confirmed in this study, neither WPSHI nor NEALI showed significant lag-1 correlations, making them unsuitable as predictors. This may be due to the weak annual persistence of high/low pressure intensity itself or the involvement of complex remote



257 forcing. Therefore, in this study, the spatial-contrast index of regional anomalies was introduced as  
258 a new predictive factor to capture more comprehensive and persistent atmospheric circulation  
259 signals.

260

261

### 262 **3.2 Simultaneous and 1-year-lagged correlations between summer atmospheric circulation** 263 **and SR-NPKP: Mechanisms and predictor design.**

264 To objectively identify optimal predictor domains, we performed an area shift experiment  
265 37., 40., 24.: for each atmospheric variable and pressure level, area-averaged anomalies were  
266 computed over the Eastern Hemisphere (10°–70°N), systematically shifting a 2.5° × 2.5° grid box  
267 in latitude and longitude. For each variable, the region yielding the maximum absolute  
268 1-year-lagged correlation with SR-NPKP was selected as the optimal predictor domain, and these  
269 regions correspond precisely to the green rectangles in Figs. 4–7.

270

#### 271 **3.2.1 Spatial structure of correlations**

272 Figs. 4-7 show the spatial patterns of simultaneous and 1-year-lagged correlations between  
273 SR-NPKP and anomalies of various atmospheric variables over the Eastern Hemisphere (10°–70°N,  
274 0°–180°E). In the following figures, climate variable abbreviations are defined as follows: SLPA -  
275 sea level pressure anomaly; GPHA - geopotential height anomaly; TA - air temperature anomaly;  
276 UA - zonal wind anomaly; and VA - meridional wind anomaly. Numerical suffixes indicate the  
277 isobaric level; for example, GPHA850 denotes the geopotential height anomaly at 850 hPa.

278 As shown in Fig. 4a, a broad region of strong negative simultaneous correlation ( $r \leq -0.50$ )  
279 exists between SR-NPKP and SLPA over continental East Asia (70°–130°E), centered near the  
280 Huai River Valley (35°N, 112.5°E). This reflects the well-documented link, highlighted in previous  
281 studies, between enhanced low-pressure/cyclonic activity over northern China and increased  
282 SR-NPKP 41., 22. A relatively weak positive correlation ( $r \approx +0.30$ ) is observed southeast of Japan  
283 (30°N, 135°E), which is thought to be associated with the westward extension of the WPSH. As the  
284 vertical level increases (from SLP to 500 hPa), both correlation centers shift toward the core region  
285 of the NEAL (45°–60°N, 110°–130°E), though the absolute magnitudes of the correlations tend to  
286 decrease (Figs. 4a, 4c, 4e, 4g). This indicates a vertically attenuating signal with baroclinic  
287 characteristics. In contrast, the 1-year-lagged correlation patterns (Figs. 4b, 4d, 4f, 4h) show that the  
288 primary negative correlation center shifts northwestward and locates over the Lake Baikal region  
289 (approximately 50°N, 95°E). Additionally, no significant positive lagged correlation is found in the  
290 northwestern Pacific. This confirms that the intensity of the WPSH in summer  $t$  does not persist into  
291 summer  $t+1$ , thus limiting its utility as a 1-year-lead predictor.



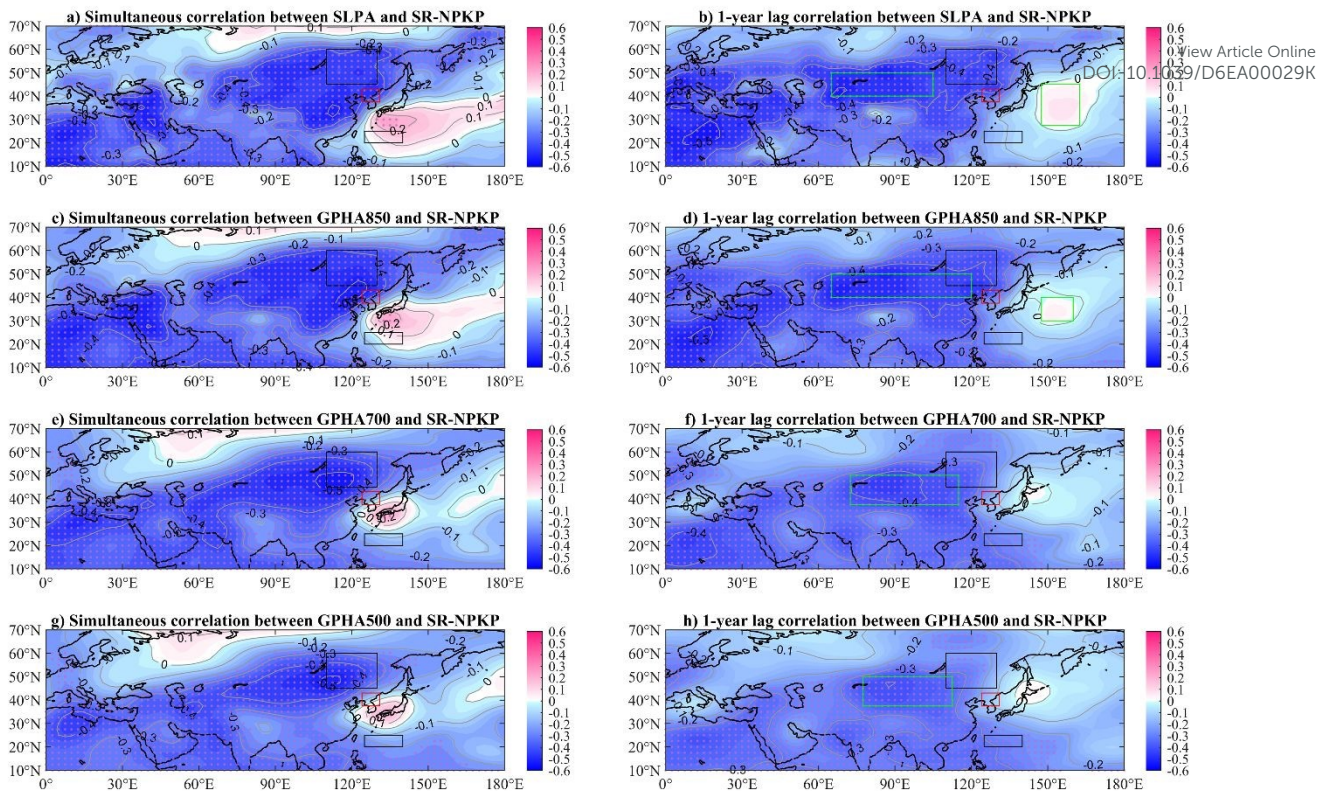


Fig. 4. Simultaneous and 1-yr lag correlation maps of SR-NPKP with SLP and GPHA in summer at 850, 700, and 500-hPa for the region of 10°–70°N in the Eastern Hemisphere. Red dots mark grid points where correlations are statistically significant ( $p < 0.05$ ). The black rectangles denote the core areas of NEAL (large) and WPSH (small), respectively. The red rectangle denotes the NPKP. The green rectangle denotes the high 1-yr lag correlation area of SR-NPKP with SLP in summer

Similar spatial displacement phenomena are observed for other atmospheric variables (Figs. 5–7). For temperature, the strongest positive simultaneous correlation appears at 850 hPa near Chengdu (30°N, 105°E) with  $r = +0.39$ , and the lagged correlation pattern shifts northwestward to peak at 850 hPa with  $r = +0.42$ . For zonal wind, enhanced westerlies over eastern China (115°–125°E) are associated with wetter summers, showing a correlation coefficient of  $r = +0.46$  at 850 hPa; the lagged correlation pattern persists despite a slight weakening, with  $r = +0.44$ . For meridional wind, both strengthened southerlies over the East Asia (132.5°E, 37.5°N;  $r = +0.45$ ) and strengthened northerlies over Krasnoyarsk (55°N, 97.5°E;  $r \approx -0.55$ ) create favorable conditions for increased SR-NPKP (Figs. 7a, g).



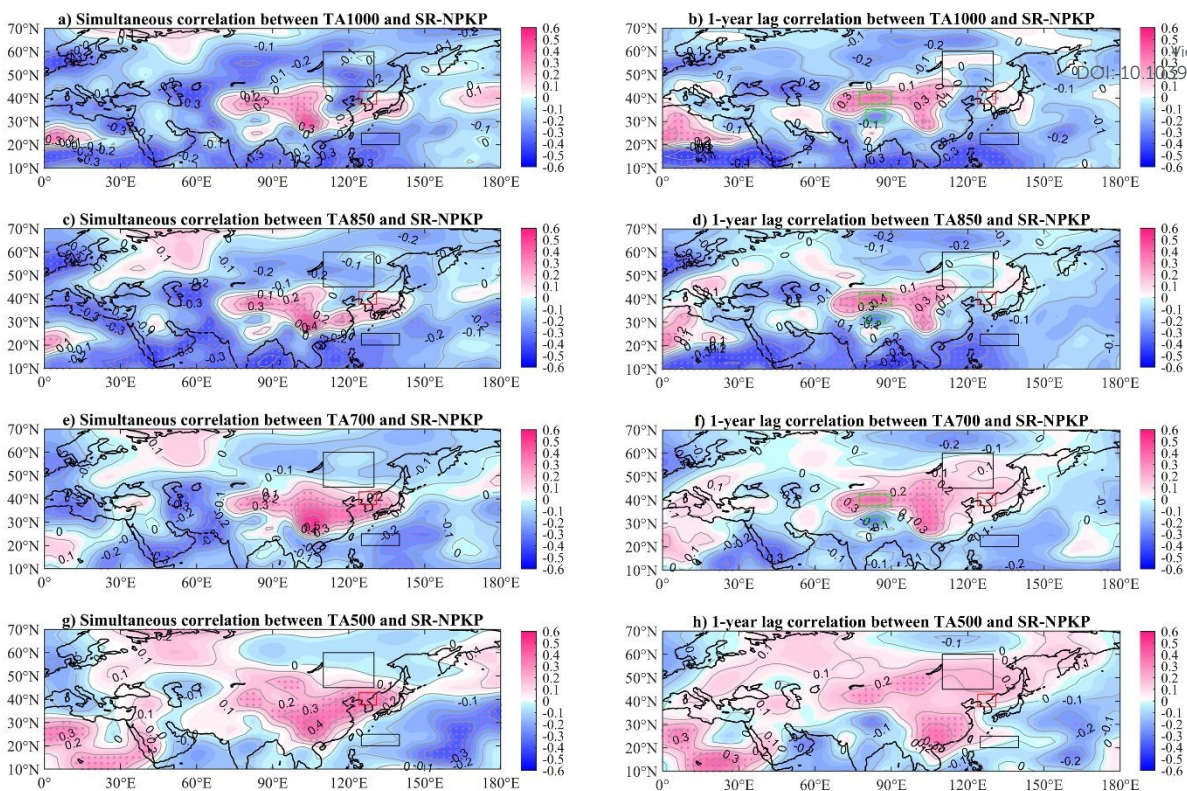


Fig. 5. The same as in Fig. 4, but with air temperature anomalies (TA) in summer at 1000, 850, 700, and 500-hPa

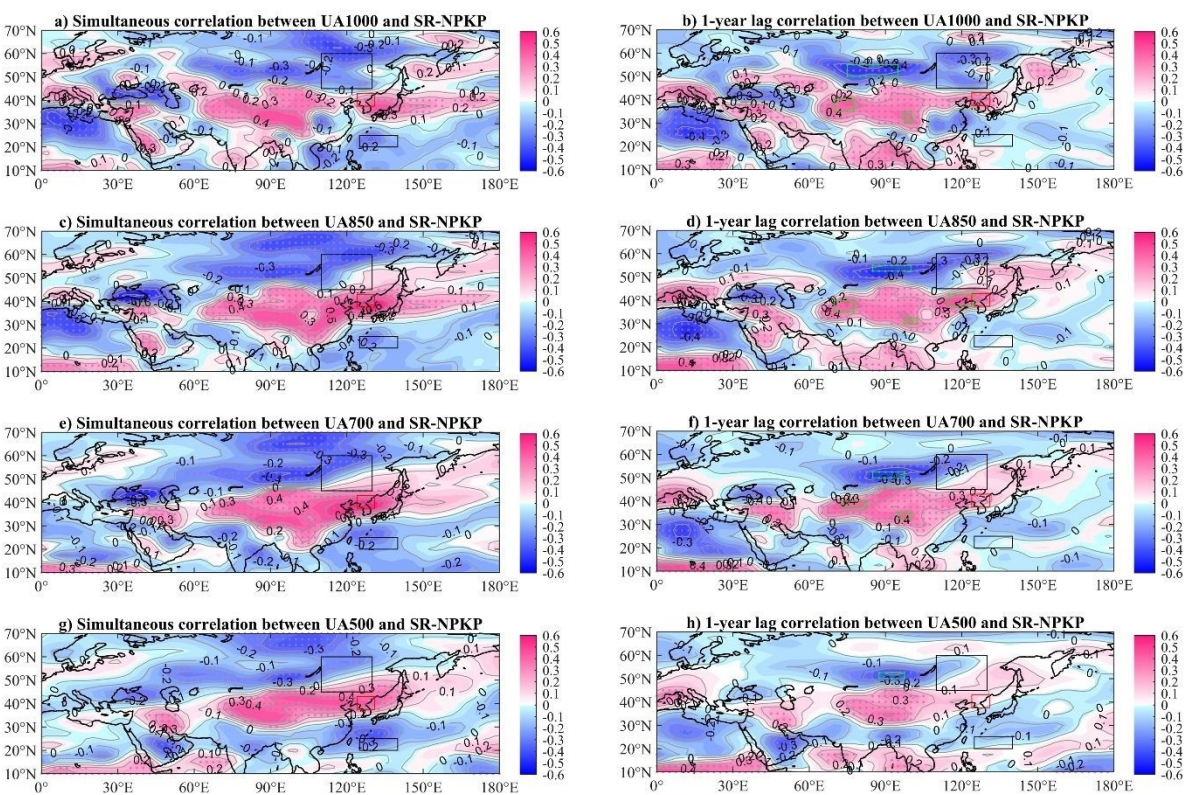


Fig. 6. The same as in Fig. 4, but with zonal wind anomalies in summer at 1000, 850, 700, and 500-hPa

Open Access Article. Published on 10 April 2026. Downloaded on 4/11/2026 1:49:21 AM. This article is licensed under a Creative Commons Attribution 3.0 Unported Licence.



309  
310  
311  
312

313  
314  
315  
316

View Article Online  
DOI: 10.1039/D6EA00029K

Environmental Science: Atmospheres Accepted Manuscript

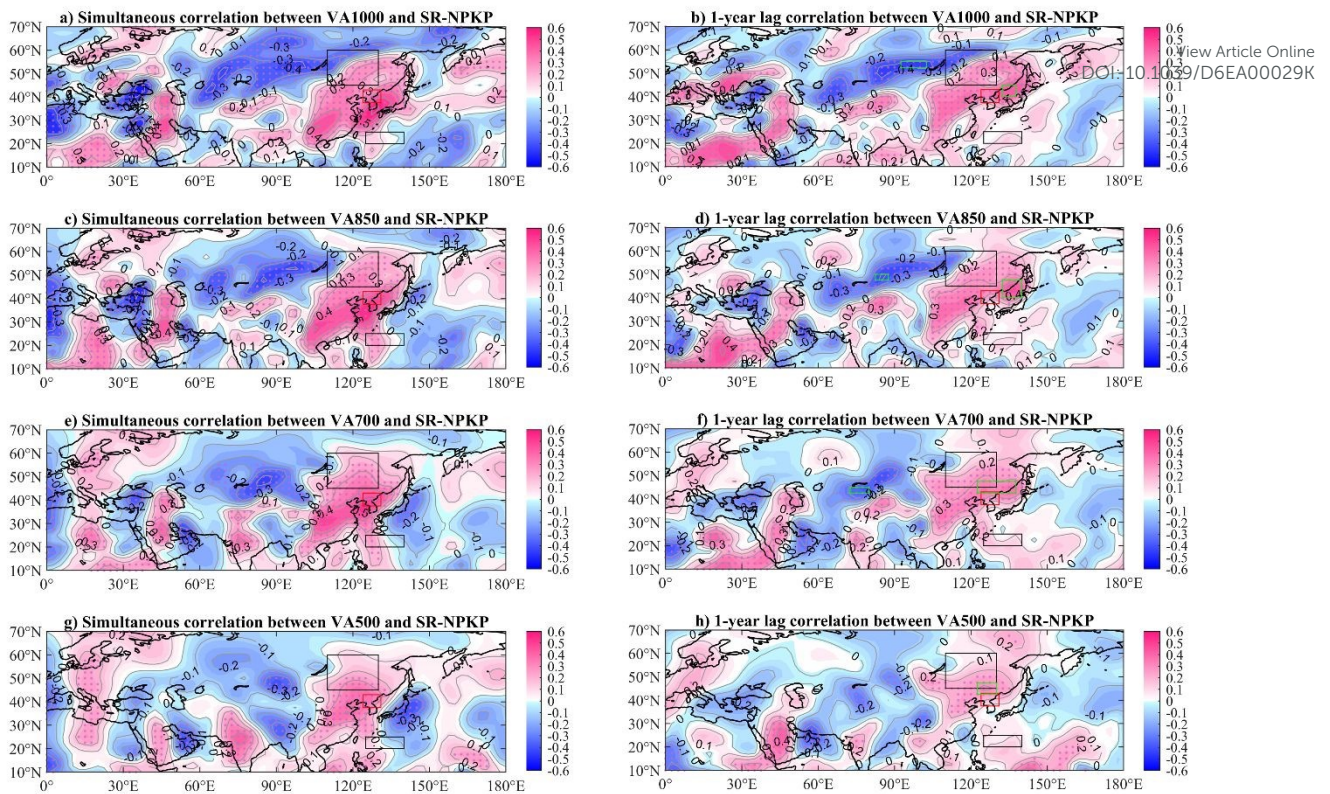


Fig. 7. The same as in Fig. 4, but with meridional wind anomalies in summer at 1000, 850, 700, and 500-hPa

### 3.2.2 Physical basis for 1-year memory

Fig. 8 schematically synthesizes the dominant atmospheric anomaly patterns in the previous summer ( $t-1$ ) that exhibit statistically significant 1-year lag correlations with SR-NPKP in year  $t$ . Specifically:

- Negative SLP and geopotential height anomalies over inland Asia ( $40^{\circ}$ – $50^{\circ}$ N,  $65^{\circ}$ – $105^{\circ}$ E) reflect a deepened low-pressure system, enhancing cyclonic circulation and low-level moisture convergence toward the Korean Peninsula. Crucially, this circulation pattern is often anchored by antecedent Eurasian snow cover anomalies that persist through the subsequent winter and spring, providing a memory bridge to summer ( $t$ ) 42.

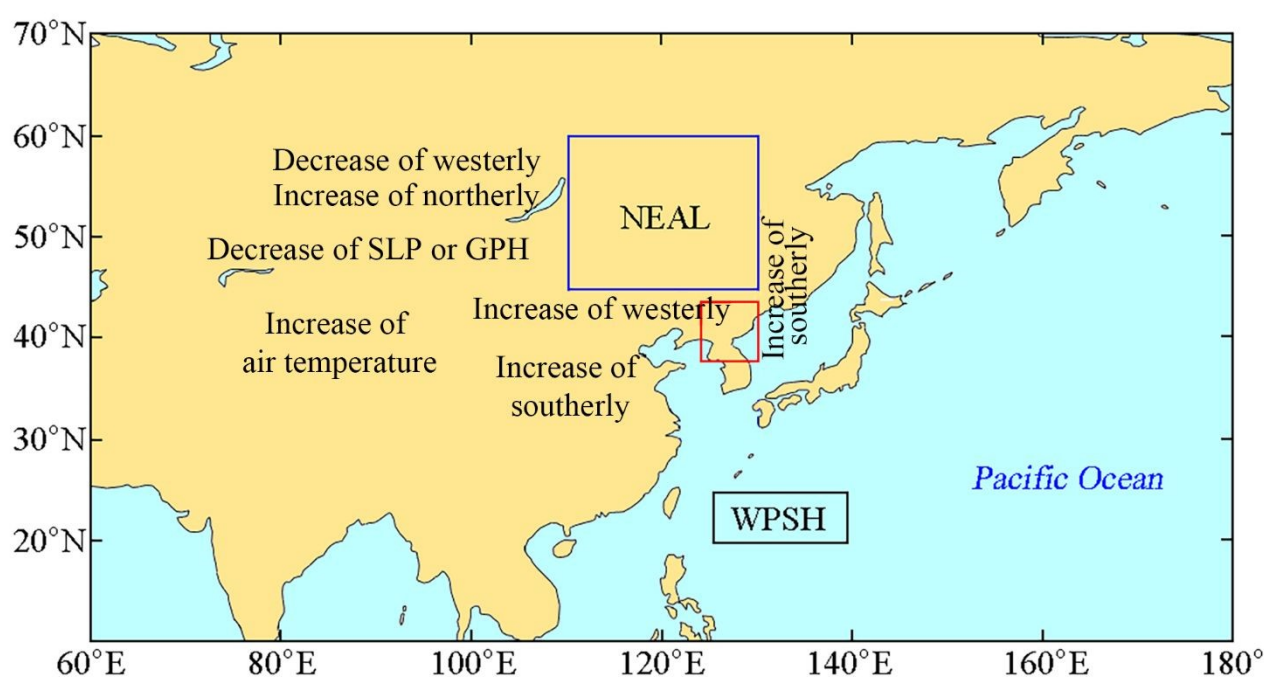
- Positive temperature anomalies over the eastern Tibetan Plateau ( $37.5^{\circ}$ – $42.5^{\circ}$ N,  $77.5^{\circ}$ – $90^{\circ}$ E) weaken the meridional thermal contrast, reducing the barrier effect of the plateau and facilitating the northward extension and persistence of the Jangma rainband 22. This thermal anomaly is sustained by soil moisture memory and subsurface heat capacity over the plateau, which decay slowly compared to atmospheric variables.

- A zonal wind dipole—enhanced westerlies over East China ( $35^{\circ}$ – $40^{\circ}$ N,  $115^{\circ}$ – $125^{\circ}$ E) and weakened westerlies over East Siberia ( $50^{\circ}$ – $55^{\circ}$ N,  $85^{\circ}$ – $100^{\circ}$ E)—strengthens the East Asian



338 subtropical jet waveguide, promoting upper-level divergence over the study region 22. The stability  
 339 of this waveguide is maintained by large-scale boundary forcings (e.g., Eurasian snow cover and  
 340 soil moisture anomalies) that lock the jet stream position across seasons.

341 – Strengthened southerly flow along a northeast–southwest corridor (Russian Far East to  
 342 southern China) and strengthened northerly flow over East Siberia ( $52.5^{\circ}$ – $55^{\circ}$ N,  $92.5$ – $102.5^{\circ}$ E)  
 343 enhance low-level moisture transport from the western Pacific while suppressing dry continental air  
 344 intrusion, favoring prolonged Jangma-front activity and heavy precipitation 2. This moisture  
 345 transport efficiency is further amplified by local soil moisture–precipitation feedback, where wet  
 346 soils from year  $t-1$  enhance evapotranspiration in year  $t$  43.



48  
 49 Fig. 8. The schematic showing the main circulation patterns in previous summer that are favorable  
 350 for the increase in SR-NPKP. The black rectangle indicates the core region of WPSH and the blue  
 351 rectangles denote the core region of NEAL. The red rectangle denotes the NPKP

352

353 To test whether these conceptual patterns reflect robust, recurrent large-scale states rather than  
 354 statistical artifacts, we conducted a composite analysis of summer ( $t-1$ ) atmospheric fields for  
 355 high-minus-low SR-NPKP years (upper vs. lower terciles of 1949–2022,  $n = 25$  per group). As  
 356 shown in Fig. 9, the composite anomalies reveal a coherent circulation structure that closely  
 357 matches the schematic in Fig. 8:

358 – A pronounced negative SLP anomaly (up to  $-2.0$  hPa) centered over Lake Baikal confirms  
 359 the intensification of a deep inland low-pressure system (Fig. 9a);

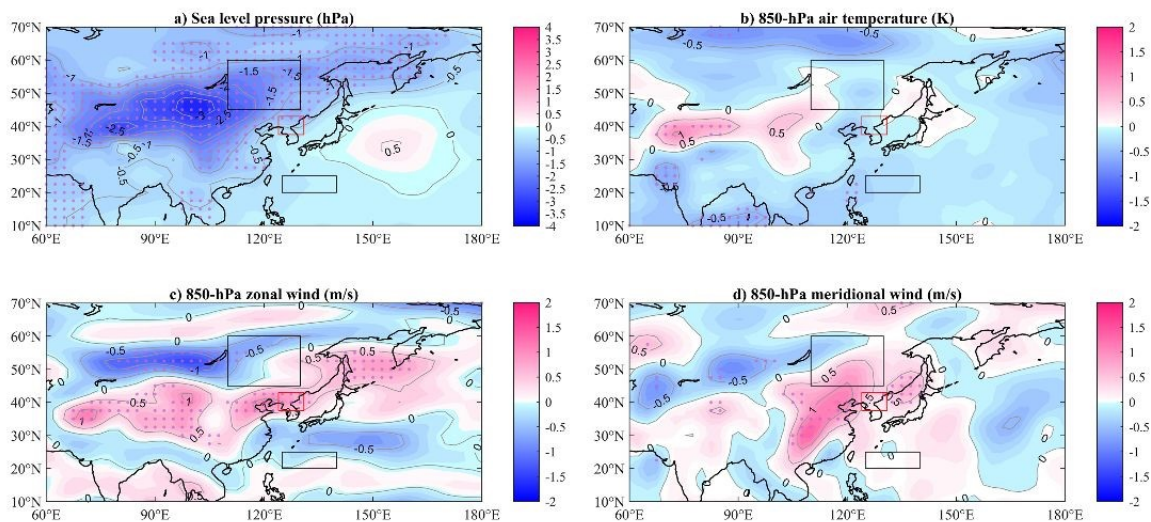
360 – Positive T850 anomalies ( $+0.8$  K) over the eastern Tibetan Plateau support thermal forcing of



361 the monsoon (Fig. 9b);

362 - Enhanced westerlies (+0.7 m/s) over eastern China and strengthened southerlies (+0.6 m/s)  
 363 along the Russian Far East coast reflect intensified low-level moisture transport (Figs. 9c, d).

364 All these features are statistically significant at the 90% confidence level (stippling,  $p < 0.10$ ,  
 365 Welch's t-test), providing strong observational validation of the proposed mechanism.



366

367 Fig. 9. Composite anomalies of summer atmospheric variables in the preceding year ( $t-1$ ) for High  
 368 minus Low SR-NPKP years (upper vs. lower terciles of 1949–2022,  $n = 25$  each). Red dots mark  
 369 grid points where correlations are statistically significant ( $p < 0.05$ ). The black rectangles denote the  
 370 core areas of NEAL (large) and WPSH (small), respectively. The red rectangle denotes the NPKP

371 While the intrinsic memory of the free atmosphere is limited to intraseasonal timescales 44.,  
 372 the atmospheric anomalies in summer ( $t-1$ ) identified in this study act as proxies for slowly varying  
 373 boundary conditions. Specifically, the deepened low-pressure system over Lake Baikal likely  
 374 reflects antecedent anomalies in soil moisture, Eurasian snow cover, or sea surface temperature,  
 375 which possess memory extending from months to years 42. These boundary forcings persist through  
 376 the winter and spring, modulating the overlying atmospheric circulation in summer ( $t$ ) via land–  
 377 atmosphere coupling and Rossby waveguide adjustments 22. Thus, the atmospheric indices selected  
 378 herein capture the integrated dynamical response to these persistent boundary forcings, rather than  
 379 representing intrinsic atmospheric memory.

380 In particular, enhanced summer precipitation in year  $t-1$  increases soil moisture over the  
 381 Korean Peninsula and surrounding Eurasian landmass. Owing to reduced evapotranspiration during  
 382 the cold season (October–April), this soil moisture anomaly decays slowly and persists into early  
 383 summer of year  $t$ , elevating low-level specific humidity and convective available potential energy  
 384 (CAPE). As demonstrated by 24., such land–atmosphere coupling provides a physically sound basis  
 385 for interannual predictability of the East Asian summer monsoon. Supporting this, 22. showed that  
 386 NEAL-related anomalies, when anchored by orography (Baikal–Okhotsk region), exhibit enhanced



387 persistence via Rossby waveguide adjustment—further stabilizing the large-scale environment  
 388 favorable for moisture transport and ascent.

View Article Online  
 DOI: 10.1039/D6EA00029K

389

### 390 3.2.3 Construction of spatial-contrast indices for 1-year prediction

391 The 1-year lag correlations between area-averaged climate variable anomalies (SLPA, GPHA,  
 392 TA, UA and VA ) in the preceding summer ( $t-1$ ) and SR-NPKP in year  $t$  are presented in Table 1.

393 These anomalies were obtained over the  $10^{\circ}$ – $70^{\circ}$ N band in the Eastern Hemisphere by shifting  
 394 calculation regions at  $2.5^{\circ}$  grid intervals. This technique is called an area shift experiment, as  
 395 described in 21., 37., and it serves to objectively identify robust correlation centers.

396

397 Table 1. Potential area-averaged climate variable anomalies in previous summer affecting the  
 398 interannual variability of SR-NPKP. The numbers behind a hyphen represent the focusing areas

Climate Variable anomaly symbol	Area	Correlation coefficient
SLPA-1	$40^{\circ}$ – $50^{\circ}$ N, $65^{\circ}$ – $105^{\circ}$ E	–0.47
SLPA-2	$27.5^{\circ}$ – $45^{\circ}$ N, $147.5^{\circ}$ – $162.5^{\circ}$ E	+0.07
GPHA850-1	$40^{\circ}$ – $50^{\circ}$ N, $65^{\circ}$ – $120^{\circ}$ E	–0.45
GPHA850-2	$30^{\circ}$ – $40^{\circ}$ N, $147.5^{\circ}$ – $160^{\circ}$ E	+0.03
GPHA700	$37.5^{\circ}$ – $50^{\circ}$ N, $72.5^{\circ}$ – $115^{\circ}$ E	–0.44
GPHA500	$37.5^{\circ}$ – $50^{\circ}$ N, $7.5^{\circ}$ – $112.5^{\circ}$ E	–0.38
TA1000-1	$37.5^{\circ}$ – $42.5^{\circ}$ N, $77.5^{\circ}$ – $90^{\circ}$ E	+0.37
TA1000-2	$30^{\circ}$ – $37.5^{\circ}$ N, $80^{\circ}$ – $87.5^{\circ}$ E	–0.23
TA850-1	$37.5^{\circ}$ – $42.5^{\circ}$ N, $77.5^{\circ}$ – $90^{\circ}$ E	+0.39
TA850-2	$30^{\circ}$ – $32.5^{\circ}$ N, $80^{\circ}$ – $87.5^{\circ}$ E	–0.25
TA700-1	$37.5^{\circ}$ – $42.5^{\circ}$ N, $77.5^{\circ}$ – $90^{\circ}$ E	+0.37
TA700-2	$30^{\circ}$ – $32.5^{\circ}$ N, $80^{\circ}$ – $87.5^{\circ}$ E	–0.26
UA1000-1	$35^{\circ}$ – $40^{\circ}$ N, $70^{\circ}$ – $77.5^{\circ}$ E	+0.45
UA1000-2	$30^{\circ}$ – $35^{\circ}$ N, $97.5^{\circ}$ – $100^{\circ}$ E	+0.42
UA1000-3	$50^{\circ}$ – $55^{\circ}$ N, $75^{\circ}$ – $95^{\circ}$ E	–0.48
UA850-1	$35^{\circ}$ – $40^{\circ}$ N, $70^{\circ}$ – $77.5^{\circ}$ E	+0.46
UA850-2	$30^{\circ}$ – $35^{\circ}$ N, $97.5^{\circ}$ – $100^{\circ}$ E	+0.42
UA850-3	$37.5^{\circ}$ – $42.5^{\circ}$ N, $115^{\circ}$ – $125^{\circ}$ E	+0.46
UA850-4	$52.5^{\circ}$ – $55^{\circ}$ N, $85^{\circ}$ – $100^{\circ}$ E	–0.47



UA700-1	37.5°–40°N, 72.5°–82.5°E	+0.48
UA700-2	32.5°–35°N, 95°–100°E	+0.44
UA700-3	50°–52.5°N, 85°–92.5°E	–0.47
UA500-1	32.5°–37.5°N, 85°–95°E	+0.39
UA500-2	50°–52.5°N, 87.5°–97.5°E	–0.41
VA1000-1	40°–45°N, 132.5°–137.5°E	+0.45
VA1000-2	52.5°–55°N, 92.5°–102.5°E	–0.46
VA850-1	40°–47.5°N, 132.5°–140°E	+0.45
VA850-2	47.5°–50°N, 82.5°–87.5°E	–0.41
VA700-1	42.5°–47.5°N, 122.5°–137.5°E	+0.42
VA700-2	42.5°–45°N, 72.5°–80°E	–0.36
VA500	42.5°–47.5°N, 122.5°–130°E	+0.33

View Article Online  
DOI: 10.1039/D6EA00029K

As shown in Table 1, individual anomalies exhibit 1-year lag correlations with SR-NPKP that range from  $-0.48$  to  $+0.48$ . However, some regions show negligible predictive skill. A typical example is GPHA850-2 over the domain  $30^{\circ}$ – $40^{\circ}$ N,  $147.5^{\circ}$ – $160^{\circ}$ E, which has a correlation coefficient of only  $+0.03$ . This poor performance likely reflects local variability that is unconnected to the Korean Peninsula. In contrast, spatial-contrast indices consistently enhance the predictive signal. These indices are defined as differences or weighted sums between regionally averaged anomalies, and the methodology has been validated for typhoon prediction in 21. In that study, differences such as SLPA-4 minus SLPA-1, which represents the pressure contrast between low pressure over North America and high pressure over the Indian Ocean, or U1000-3 minus U1000-2, which captures westerly shear, were shown to better capture large-scale oscillation patterns. These patterns include phenomena like land–ocean pressure seesaws and meridional wind shear, and the indices perform better than single-region averages by suppressing local noise and improving the signal-to-noise ratio.

Following a physics-based approach, this study generated candidate indices via linear combinations of regionally averaged anomalies—using differences for dipole patterns and weighted sums for tripole patterns. All mathematically possible pairwise and tripole combinations among the 13 candidate regions identified through the area-shift experiment were systematically evaluated against the statistical significance threshold ( $|r| \geq 0.40$ ,  $p < 0.001$ ,  $n = 74$ ). Exactly 13 combinations satisfied this criterion and were retained without further subjective filtering. Notably, all retained indices exhibited physically coherent spatial patterns (e.g., pressure gradients between inland Eurasia and the Northwest Pacific), indicating that physical interpretability emerged naturally as a



399

400

401

402

403

404

405

406

407

408

409

410

411

412

413

414

415

416

417

418

419

420

421 property of statistically significant predictors rather than serving as an additional selection criterion  
 422 (Table 2).

View Article Online  
 DOI: 10.1039/D6EA00029K

423 This data-driven refinement is exemplified by the first index (SLP\_D12), which quantifies the  
 424 sea level pressure contrast not between the a priori defined WPSH and NEAL domains, but between  
 425 the two regions exhibiting the strongest lagged signals: inland Eurasia (40°–50°N, 65°–105°E) and  
 426 the Northwest Pacific (27.5°–45°N, 147.5°–162.5°E). While the conventional WPSH–NEAL  
 427 intensity difference aligns reasonably well with simultaneous circulation–precipitation relationships  
 428 (Fig. 4a), its 1-year-lagged correlation is markedly limited, as the dominant signal shifts  
 429 northwestward toward the Lake Baikal region in lagged correlation fields (Figs. 4b, 4d, 4f, 4h). In  
 430 contrast, SLP\_D12 captures this spatially extended pressure gradient involving inland Eurasia and  
 431 achieves an enhanced absolute correlation coefficient of  $|r| = 0.49$ . This illustrates how regionally  
 432 optimized spatial contrasts, grounded in observed lagged teleconnections, can improve upon  
 433 traditional indices that rely on fixed climatological domains.

434 The eighth index (U850\_D1234) quantifies the spatial asymmetry between strengthened  
 435 low-level westerlies over three adjacent regions in eastern China (35°–42.5°N, 70°–125°E) and  
 436 weakened background westerlies over central Siberia (52.5°–55°N, 85°–100°E). This structure  
 437 physically aligns with the mechanism of NEAL intensification accelerating jet waveguide  
 438 acceleration as proposed by 22. It also exhibits the highest one-year-lagged correlation with  
 439 SR-NPKP ( $r = +0.52$ ,  $p < 0.001$ ). The eleventh index (V1000\_D12) represents the combination of  
 440 enhanced southerly winds along the eastern coast of the Korean Peninsula and enhanced northerly  
 441 winds over central Siberia. This pattern is consistent with the low-level moisture transport  
 442 mechanism sustaining the Jangma front, as described by 2. It is thus interpreted as a low-level  
 443 moisture transport index.

445 Table 2. Potential spatial-contrast indices of area-averaged climate variable anomalies  
 446 connected with the interannual variability of SR-NPKP

Number	Definition	Symbol	Correlation coefficient
1	SLPA-1 – SLPA-2	SLP_D12	–0.49
2	GPHA850-1 – GPHA850-2	GPHA850_D12	–0.47
3	GPHA700	GPHA700	–0.44
4	TA1000-1 – TA1000-2	T1000_D12	+0.43
5	TA850-1 – TA850-2	T850_D12	+0.45
6	TA700-1 – TA700-2	T700_D12	+0.43



7	UA1000-1 + UA1000-2 – UA1000-3	U1000_D123	+0.50
8	UA850-1 + UA850-2 + UA850-3 – UA850-4	U850_D1234	+0.52
9	UA700-1 + UA700-2 – UA700-3	U700_D123	+0.52
10	UA500-1 – UA500-2	U500_D12	+0.43
11	VA1000-1 – VA1000-2	V1000_D12	+0.49
12	VA850-1 – VA850-2	V850_D12	+0.48
13	VA700-1 – VA700-2	V700_D12	+0.43

View Article Online

DOI: 10.1039/D6EA00029K

### 3.3. Prediction experiments of SR-NPKP for annual leadtime and analyses of results

The central question of this study is which subset of predictors yields the highest prediction skill for SR-NPKP at an annual lead time using BPNN. Predictor selection for the neural network model was performed based on predictive performance derived from 5-fold cross-validation. Various predictor combinations were constructed using the 13 potential spatial-contrast indices listed in Table 2, and performance metrics including anomaly correlation coefficient (ACC), root-mean-square error (RMSE), and mean bias error (MBE) were evaluated. Accordingly, the top 5 best-performing predictor sets were selected for detailed analysis (Table 3), in which the performance metrics of the linear regression model using the same predictors are also presented for comparison.

For each predictor set, a BPNN with the logistic sigmoid activation function was employed. Model training and validation were implemented via 5-fold cross-validation over the full period 1949–2022, where each fold uses 4/5 of the time series for training and 1/5 for validation. Considering the sensitivity of neural network training to initial random weights, 100 repeated runs with different random seeds were conducted for each predictor set. The model achieving the lowest cross-validation RMSE was selected as the representative model for each set.

Performance metrics (ACC, RMSE, MBE) were calculated by concatenating the predicted and observed values from all five validation folds of the 5-fold cross-validation (1949–2022), thereby representing the model's skill over the entire period. The top 5 predictor combinations are ranked by BPNN ACC.  $\Delta$ ACC and  $\Delta$ RMSE denote the improvement of BPNN over MLR (positive  $\Delta$ ACC and negative  $\Delta$ RMSE indicate BPNN superiority). The optimal predictor set (Case 3) is highlighted in bold.

Table 3. Comparison of prediction performance between BPNN and Multiple Linear Regression (MLR) models using identical predictor sets.

Case	Set of predictors	BPNN			MLR			$\Delta$ (BPNN-MLR)
		ACC	RMSE	MBE	ACC	RMSE	MBE	$\Delta$ ACC / $\Delta$ RMSE



1	V850_D12, SLP_D12, T700_D12, U1000_D123	0.54	139.08	-7.64	0.32	157.81	3.29	+0.22 / -18.73
2	V850_D12, T850_D12, U850_D1234, U500_D12	0.53	140.15	2.13	0.41	152.03	1.46	+0.12 / -11.88
3	<b>V850_D12, SLP_D12, T850_D12, U850_D1234</b>	0.59	134.61	-4.22	0.53	140.41	1.83	+0.06 / -5.80
4	V850_D12, T850_D12, GPHA700, U850_D1234	0.54	138.96	-6.63	0.38	154.64	5.27	+0.16 / -15.68
5	V850_D12, T850_D12, GPHA700, U850_D1234, U500_D12	0.53	140.19	3.04	0.40	153.74	4.33	+0.13 / -13.55

View Article Online  
DOI: 10.1039/D6EA00029K

As shown in Table 3, in terms of the ACC and RMSE metrics, the BPNN consistently outperforms the MLR across all five predictor combinations. Under the optimal predictor set (Case 3: V850\_D12, SLP\_D12, T850\_D12, U850\_D1234), the BPNN achieves the highest ACC of 0.59 and the lowest RMSE of 134.61 mm, whereas the MLR yields an ACC of 0.53 and an RMSE of 140.41 mm with the same predictors. The performance gap ( $\Delta\text{ACC} = +0.06$ ,  $\Delta\text{RMSE} = -5.80$  mm) confirms that even when well-selected predictors are used, nonlinear modeling provides additional predictive performance improvement. At this time, the optimal predictor set obtained above includes the meridional wind index (V850\_D12), sea-level pressure index (SLP\_D12), low- to mid-tropospheric temperature index (T850\_D12), and zonal wind index (U850\_D1234).

Notably, the advantage of BPNN becomes more pronounced for suboptimal predictor combinations. For instance, in Case 1, BPNN achieves  $\Delta\text{ACC} = +0.22$  and  $\Delta\text{RMSE} = -18.73$  mm relative to MLR, suggesting that BPNN better captures nonlinear interactions among atmospheric variables that linear models cannot represent. Regarding systematic bias, both models exhibit small MBE values ( $|\text{MBE}| < 8$  mm) across all cases, indicating minimal systematic over- or under-prediction. These results confirm that the superiority of BPNN stems from its ability to model complex, nonlinear relationships among circulation predictors, rather than merely from using multiple inputs.

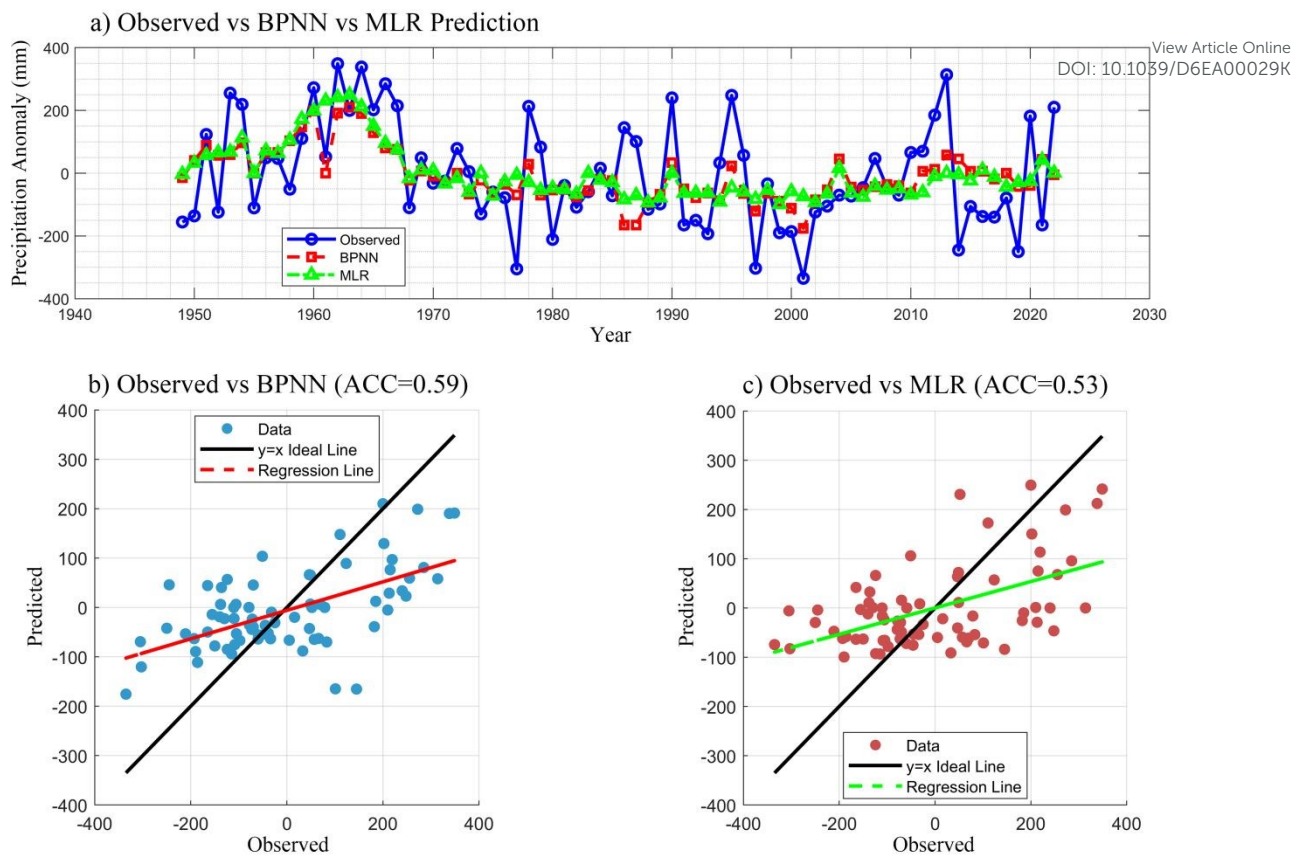


Fig. 10. Prediction performance of the BPNN model using the optimal predictor set (Case 3: V850\_D12, SLP\_D12, T850\_D12, U850\_D1234) over the full period 1949–2022.

Fig. 10 illustrates the prediction performance of BPNN using the optimal predictor set (Case 3: V850\_D12, SLP\_D12, T850\_D12, U850\_D1234) over the full period (1949–2022). Panel (a) shows the time series of observed precipitation anomalies alongside BPNN (red squares) and MLR (green triangles) predictions, while panels (b) and (c) present scatter plots with corresponding ACC values.

The time series comparison (Fig. 10a) reveals that both BPNN and MLR models reasonably capture the general phase of interannual variability, demonstrating the practical utility of these models for seasonal to interannual rainfall prediction. However, both models exhibit systematic limitations in predicting extreme events. While BPNN shows slightly greater variability than MLR, both models substantially underestimate precipitation anomalies during extreme wet years (e.g., early 1960s: 1960, 1962, 1964, 1966; mid-1990s: 1990, 1995; 2013) and substantially overestimate precipitation anomalies during extreme dry years (e.g., 1974, 1977, 1980, 1997, 2001, 2014, 2019). The differences for these extreme events often exceed 150 mm, indicating that neither model adequately captures the full amplitude of precipitation variability. Notably, however, the prediction errors for extreme events are notably reduced in BPNN compared to MLR.



510 To complement the continuous metrics and provide more operationally relevant guidance, we  
511 also evaluated categorical prediction skill using the Heidke Skill Score (HSS) 45. Following the  
512 WMO standardized verification system for long-range forecasts 46., observed and predicted  
513 precipitation anomalies were classified into three equiprobable tercile categories: Below Normal  
514 (<33rd percentile), Near Normal (33rd–67th percentile), and Above Normal (>67th percentile).

515 The results show that BPNN achieves an overall HSS of 0.236, which represents a  $\Delta$ HSS of  
516 +0.10 compared to MLR (HSS = 0.136), corresponding to a 73.5% relative improvement. This  
517 indicates that the BPNN model provides statistically superior predictive skill for seasonal rainfall  
518 categorical forecasting compared to MLR. This categorical assessment reveals an important  
519 nuance: while both models struggle to capture the exact amplitude of extreme precipitation events  
520 in continuous space (as evidenced by the regression-to-the-mean effect in Fig. 10b–c), they  
521 nonetheless provide skillful guidance for predicting the general direction of seasonal anomalies  
522 (above or below normal). For operational users—such as agricultural planners, water resource  
523 managers, and disaster preparedness agencies—this categorical information is often more  
524 actionable than precise quantitative forecasts. The BPNN's modest but meaningful improvement  
525 over MLR ( $\Delta$ HSS = +0.10, or 74% relative increase) further underscores the value of nonlinear  
526 modeling for capturing complex circulation–precipitation relationships that linear approaches may  
527 miss.

528 Nevertheless, users should exercise caution when interpreting predictions for years with  
529 potentially extreme rainfall conditions, as both models exhibit systematic underestimation of  
530 extreme wet events and overestimation of extreme dry events. Future enhancements, such as  
531 incorporating direct moisture predictors (e.g., specific humidity at 850 hPa, precipitable water) or  
532 adopting probabilistic forecasting frameworks, may further improve skill for extreme-event  
533 prediction.

534 The scatter plots (Fig. 10b–c) confirm this limitation. Although BPNN achieves a higher  
535 ACC (0.59) compared to MLR (0.53), the marginal improvement of +0.06 indicates that while  
536 BPNN captures slightly more variance than MLR, the improvement is limited. Both models  
537 exhibit regression lines with slopes substantially less than unity, reflecting a strong tendency to  
538 shrink predictions toward the climatological mean. This "regression to the mean" effect is  
539 particularly severe for extreme events ( $|\text{anomaly}| > 150$  mm), where data points deviate  
540 substantially from the 1:1 line in both models.

541 Despite these limitations, the ACC values of 0.53–0.59 are noteworthy for seasonal to  
542 interannual prediction, as precipitation is inherently more difficult to predict than temperature due  
543 to its high spatiotemporal variability. For operational seasonal forecasting purposes, these models  
544 provide operationally useful information for predicting the general direction of seasonal rainfall



545 anomalies (above or below normal), which is valuable for agricultural planning, water resource  
546 management, and disaster preparedness. Nevertheless, users should exercise caution when  
547 interpreting predictions for years with potentially extreme rainfall conditions.

548 Although the optimal predictor set (Case 3) does not include explicit moisture-related  
549 predictors, the wind, temperature and pressure-based indices (V850\_D12, SLP\_D12, T850\_D12,  
550 U850\_D1234) are dynamically linked to atmospheric circulation patterns. However, the  
551 systematic misrepresentation of extremes suggests that these circulation indices alone may not  
552 fully capture the complex boundary-layer atmosphere interactions (e.g., soil moisture feedback,  
553 typhoon interactions, convective processes) that amplify extreme precipitation events. The absence  
554 of direct moisture predictors (e.g., specific humidity at 850 hPa, precipitable water) may further  
555 limit the models' ability to capture extreme wet events, which often depend critically on moisture  
556 availability and convective instability.

557 While this study demonstrates that atmospheric circulation precursors—particularly  
558 regionally optimized spatial-contrast indices—provide statistically significant skill for 1-year-lead  
559 prediction of SR-NPKP, we acknowledge that boundary forcings may contribute additional  
560 predictability at this lead time. In particular, sea surface temperature anomalies (e.g., ENSO),  
561 Eurasian snow cover, and soil moisture memory have been documented as sources of  
562 interannual-to-decadal climate predictability in the East Asian monsoon system [42.](#), [24.](#), [43.](#)

563 However, two practical considerations motivated our focus on atmospheric indices in the  
564 present work. First, the observational record for reliable land surface variables (e.g., in situ soil  
565 moisture, snow depth) over inland Eurasia remains sparse prior to the satellite era (pre-1980s),  
566 limiting robust multi-decadal analysis with our 74-year dataset (1949–2022). Second, preliminary  
567 analysis revealed that direct lag-1 correlations between SR-NPKP and canonical ENSO indices  
568 (e.g., Niño3.4) are weak, consistent with previous findings that ENSO's teleconnection to East  
569 Asian climate is highly nonlinear, shows complex variations, and is strongly modulated by  
570 extratropical circulation patterns [47.](#) In contrast, the spatial-contrast indices developed herein  
571 capture circulation configurations that integrate both tropical and extratropical influences, yielding  
572 substantially higher lag-1 correlations ( $|r| \geq 0.40$ ).

573 We therefore interpret atmospheric circulation not as a substitute for boundary forcings, but  
574 as an integrated dynamical response that partially reflects the memory of prior boundary  
575 conditions. Future work will explicitly incorporate reanalysis-based boundary variables (e.g.,  
576 ERA5-Land soil moisture, EASE-Grid snow water equivalent) and phase-resolved ENSO indices  
577 into a hybrid predictor system. Such integration may further enhance prediction skill, particularly  
578 for extreme events where boundary-atmosphere coupling plays a dominant role.

579 In addition to predictor limitations, spatial scale limitations exist. While this study



580 demonstrates skillful prediction for the regional mean precipitation over the NPKP, there are  
581 limitations regarding sub-regional scales. Precipitation variability at smaller spatial scales is often  
582 governed by local topography and convective processes that are not fully captured by large-scale  
583 circulation indices. Additionally, the limited sample size (74 years) poses challenges for  
584 developing robust independent models for multiple sub-regions without overfitting. Consequently,  
585 future work will aim to address these issues by incorporating higher-resolution observational data  
586 and local terrain factors to enhance predictive skill at sub-regional scales.

587

#### 588 4. Conclusion

589 This study establishes a regionally tailored framework for 1-year-lead prediction of summer  
590 precipitation over the northern part of the Korean Peninsula (NPKP). The principal findings and  
591 their implications are summarized below.

592 First, traditional circulation indices such as WPSHI and NEALI exhibit negligible lag-1  
593 correlations ( $|r| < 0.2$ ) with SR-NPKP, confirming their limited utility for annual-lead forecasting.  
594 However, simultaneous and 1-year-lagged correlation analyses reveal a pronounced northwestward  
595 shift of the dominant signal from the canonical WPSH–NEAL dipole in summer ( $t$ ) to a  
596 Baikal-centered low-pressure anomaly in summer ( $t-1$ ). This shift indicates that interannual  
597 predictability resides in spatially displaced pressure–wind configurations over inland Eurasia rather  
598 than in fixed climatological domains.

599 Second, guided by this physical insight, an objective area-shift experiment identified robust  
600 lagged precursors across the Eastern Hemisphere ( $10^{\circ}$ – $70^{\circ}$ N). Thirteen spatial-contrast indices  
601 constructed as linear combinations of regionally averaged circulation anomalies were screened for  
602 statistically significant lag-1 correlations ( $|r| \geq 0.40$ ,  $p < 0.001$ ). The sea level pressure contrast  
603 index SLP\_D12, quantifying the pressure difference between the Baikal low ( $40^{\circ}$ – $50^{\circ}$ N,  $65^{\circ}$ –  
604  $105^{\circ}$ E) and the Northwest Pacific high ( $27.5^{\circ}$ – $45^{\circ}$ N,  $147.5^{\circ}$ – $162.5^{\circ}$ E), achieves  $|r| = 0.49$  and  
605 substantially outperforms raw area-mean predictors.

606 Third, a BPNN using four optimal predictors (V850\_D12, SLP\_D12, T850\_D12,  
607 U850\_D1234) yields an anomaly correlation coefficient (ACC) of 0.59, a root mean square error  
608 (RMSE) of 134.61 mm, and a mean bias error (MBE) of  $-4.22$  mm over the 5-fold cross-validation  
609 period (1949–2022), significantly outperforming multiple linear regression benchmarks (ACC =  
610 0.53, RMSE = 140.41 mm) using identical predictors. The performance gap ( $\Delta$ ACC = +0.06,  
611  $\Delta$ RMSE =  $-5.80$  mm) confirms that nonlinear modeling provides additional predictive skill even  
612 when well-selected predictors are used. Wind-based indices dominate the optimal set, consistent  
613 with their dynamical linkage to underlying pressure gradients and moisture transport pathways.

614 Fourth, while this study demonstrates skillful prediction for regional mean precipitation, we



615 acknowledge limitations regarding sub-regional scales and boundary variable integration.  
616 Precipitation variability at smaller spatial scales is often governed by local topography and  
617 convective processes that are not fully captured by large-scale circulation indices. Additionally, the  
618 limited sample size (74 years) poses challenges for developing robust independent models for  
619 multiple sub-regions without overfitting. Future work will aim to address these issues by  
620 incorporating higher-resolution observational data, reanalysis-based boundary variables (e.g.,  
621 ERA5-Land soil moisture, EASE-Grid snow water equivalent), and phase-resolved ENSO indices  
622 into a hybrid predictor system.

623 Finally, this work demonstrates that regionally optimized spatial contrasts of atmospheric  
624 circulation provide superior predictive skill for monsoon precipitation compared to global-scale  
625 indices, offering a transferable strategy for long-lead forecasting in data-scarce regions. The  
626 methodology developed herein can be adapted to other monsoon-dependent regions where  
627 observational networks are sparse but reanalysis data are available, contributing to improved  
628 climate resilience and disaster preparedness in vulnerable communities.

629 **CRedit** authorship contribution statement **Yong-Sik Ham**: Visualization, Investigation, Data  
630 curation. **Hyon-Su Ri**: Software, Writing – original draft. **Kyong-Bok Sonu**: Software,  
631 Visualization. **Sang-Il Jong**: Conceptualization, Methodology. **Un Sim Paek**: Supervision.

632 **Conflicts of interest** The authors declare no conflicts of interest.

### 633 **Data availability statement**

634 Data are available from the corresponding author upon request.

### 635 **Acknowledgments**

636 We are grateful to the State Hydro-Meteorological Administration (SHMA) of DPR of Korea for  
637 providing the observational monthly precipitation data of the DPRK.

### 638 **References**

- 639 1. Zhang, R., 2015: Changes in East Asian summer monsoon and summer precipitation over eastern  
640 China during recent decades. *Sci. Bull.*, 60(13), 1222–1224.
- 641 2. Om, K.C., G. Ren, S. Li, and K.C. O, 2018: Climatological characteristics and long-term  
642 variation of rainy season and torrential rain over DPR Korea. *Wea. Clim. Extremes*, 28, 667–  
643 678.



- 650 3. Fang, Y., Y. Zhang, A. Huang, and B. Li, 2013: Seasonal and intraseasonal variations of East  
651 Asian summer monsoon precipitation simulated by a regional air–sea coupled model. *Adv.*  
652 *Atmos. Sci.*, 30, 315–329. View Article Online  
DOI: 10.1002/asl.10029K
- 653 4. Ding, Y. H., and J. C. L. Chan, 2005: The East Asian summer monsoon: an overview. *Meteorol.*  
654 *Atmos. Phys.*, 89, 117–142.
- 655 5. Guan, W. N., X. J. Ren, W. Shang et al., 2018: Subseasonal zonal oscillation of the western  
656 Pacific subtropical high during early summer. *J. Meteorol. Res.*, 32(5), 768–780.
- 657 6. Kripalani, R. H., and A. Kulkarni, 2001: Monsoon precipitation variations and teleconnections  
658 over South and East Asia. *Int. J. Climatol.*, 21, 603–616.
- 659 7. Wang, B., and H. Lin, 2002: Rainy season of the Asian-Pacific summer monsoon. *J. Climate*, 15,  
660 386–396.
- 661 8. Huang, Y., and X. Li, 2015: The interdecadal variation of the western Pacific subtropical high as  
662 measured by 500 hPa eddy geopotential height. *Atmos. Oceanic. Sci. Lett.*,  
663 doi:10.3878/AOSL20150038.
- 664 9. Huang, Y. B., X. Wang, X. Li, and H. Wang., 2018: Changes in the influence of the western  
665 Pacific subtropical high on Asian summer monsoon precipitation in the late 1990s. *Clim. Dyn.*,  
666 51, 443–455.
- 667 10. Ali, M. M., Nagamani, P. V., Sharma, N., Venu Gopal, R. T., Rajeevan, M., Goni, G. J., &  
668 Bourassa, M. A., 2015: Relationship between ocean mean temperatures and Indian summer  
669 monsoon precipitation. *Atmos. Sci. Lett.*, 16(3), 408–413. <https://doi.org/10.1002/asl2.576>
- 670 11. Venugopal, T., Ali, M. M., Bourassa, M. A., Zheng, Y., Goni, G. J., Foltz, G. R., & Rajeevan,  
671 M., 2018: Statistical evidence for the role of southwestern Indian Ocean heat content in the  
672 Indian summer monsoon precipitation. *Sci. Rep.*, 8, 12092.  
673 <https://doi.org/10.1038/s41598-018-30552-0>
- 674 12. Venugopal, T., Rahaman, H., Anna, R., Erik, S., Ravichandran, M., Ramakrishna, S. S. V. S.,  
675 2023: Quantifying the role of antecedent Southwestern Indian Ocean capacitance on the  
676 summer monsoon precipitation variability over homogeneous regions of India. *Sci. Rep.*, 13,  
677 5553. <https://doi.org/10.1038/s41598-023-32840-w>
- 678 13. Kurian, N., Venugopal, T., Singh, J., & Ali, M. M., 2017: A soft-computing ensemble approach  
679 (SEA) to forecast Indian summer monsoon precipitation. *Meteorol. Appl.*, 24(2), 308–314.  
680 <https://doi.org/10.1002/met.1650>
- 681 14. Hu, Z.Z., 1997: Interdecadal variability of summer climate over East Asia and its association  
682 with 500hPa height and global sea surface temperature. *J. Geophys. Res.*, 102, 19, 403–19, 412.
- 683 15. Chen, Y., H. Zhang, R. Zhou, and H. Wu, 2001: Relationship between the ground surface  
684 temperature in Asia and the intensity and location of subtropical high in the western Pacific.



- 685 Chin. J. Atmos. Sci., 25, 515–522.
- 686 16. Yuan, Y., H. Gao, W. Li, Y. Liu, L. Chen, B. Zhou, and Y. Ding, 2017: The 2016 summer  
687 floods in China and associated physical mechanisms: A comparison with 1998. *J. Meteor. Res.*,  
688 31, 261–277.
- 689 17. Ren, H.L., J. Zuo, and Y. Deng, 2019: Statistical predictability of Niño indices for two types of  
690 ENSO. *Clim. Dyn.*, 52, 5361–5382.
- 691 18. Fan, K., Y. Liu, and H. Chen, 2012: Improving the Prediction of the East Asian Summer  
692 Monsoon: New Approaches. *Wea. Forecasting*, 27, 1017–  
693 1030. <https://doi.org/10.1175/WAF-D-11-00092.1>
- 694 19. Gong, H., L. Wang, W. Chen, R. Wu, K. Wei, and X. Cui, 2014: The climatology and  
695 interannual variability of the East Asian winter monsoon in CMIP5 models. *J. Clim.*, 27,  
696 1659–1678. <https://doi.org/10.1175/JCLI-D-13-00039.1>
- 697 20. Hu, W., P. Liu, Q. Zhang, and B. He, 2019: Dominant patterns of winter-time intraseasonal  
698 surface air temperature over the CONUS in response to MJO convections. *Clim. Dyn.*, 53,  
699 3917–3936.
- 700 21. Jong, S. I., Y. S. Ham, K. C. Om, U. S. Paek, and S. S. O, 2022: Seasonal prediction of  
701 typhoons approaching the Korean Peninsula using several statistical methods. *Natural Hazards*,  
702 doi:10.1007/s11069-022-05450-4.
- 703 22. Lin, Z., and B. Wang, 2016: Northern East Asian low and its impact on the interannual variation  
704 of East Asian summer rainfall. *Clim. Dyn.*, 46, 83–97.
- 705 23. Lee, E., N. Thomas, T. N. Chase, and B. Rajagopalan, 2007: Seasonal forecasting of East Asian  
706 summer monsoon based on oceanic heat sources. *Int. J. Climatol.*, 28, 667–678.
- 707 24. Wu, Z., B. Wang, J. Li, F. F. Jin, 2009: An empirical seasonal prediction model of the east  
708 Asian summer monsoon using ENSO and NAO. *J. Geophys. Res.*, 114: D18120.  
709 doi:10.1029/2009JD011733.
- 710 25. Wang, L., M. Ting, D. Chapman, D. E. Lee, N. Henderson, and X. Yuan, 2016: Prediction of  
711 northern summer low–frequency circulation using a high–order vector auto–regressive model.  
712 *Clim Dyn.*, 46, 693–709.
- 713 26. Hornik, K., M. Stichcombe, and H. White, 1989: Multi-layer feedforward networks are  
714 universal approximators. *Neural Networks*, 2, 359–366.
- 715 27. Zhang, G., B. E. Patuwo, and M.Y. Hu, 1998: Forecasting with artificial neural networks: The  
716 state of the art. *Int. J. Forecasting*, 14, 35–62.
- 717 28. Yakut, E., and S. Süzülmüş, 2020: Modelling monthly mean air temperature using artificial  
718 neural network, adaptive neuro-fuzzy inference system and support vector regression methods:  
719 A case of study for Turkey. *Computation in Neural Systems*, 31, 1-36.

View Article Online  
DOI: 10.1039/C9EM00299K



- 720 29. Lockwood, J. F., H. E. Thornton, N. Dunstone, A. A. Scaife, P. E. Bett, C. Li, and H. L. Ren,  
 721 2019: Skilful seasonal prediction of winter wind speeds in China. *Clim. Dyn.*, 53, 3937–3955. View Article Online  
 3937-3955-0029K
- 722 30. Woli, P., J. Jones, K. Ingram, and J. Paz, 2013: Forecasting drought using the agricultural  
 723 reference index for drought (ARID): A case study. *Wea. Forecasting*, 28, 427–443.
- 724 31. Wang, L., X. Yuan, and C. Li, 2019: Subseasonal forecast of Arctic sea ice concentration  
 725 via statistical approaches. *Clim. Dyn.*, 52, 4953–4971.
- 726 32. Kalnay, E., and M. Kanamitsu, and R. Kistler, and W. Collins, ..., and D. Joseph, 1996: The  
 727 NCEP/NCAR 40-year reanalysis project. *Bull. Amer. Meteor. Soc.*, 77, 437–471.
- 728 33. He, X., and D. Gong, 2002: Interdecadal change in western Pacific subtropical high and climatic  
 729 effects. *J. Geogr. Sci.*, 12(2), 202–209.
- 730 34. WMO, 1966: Climatic Change, WMO Technical Note No. 79, WMO No. 195-TP-100, World  
 731 Meteorological Organization, Geneva.
- 732 35. Mann, H. B., 1945: Nonparametric tests against trend. *Econometrica*. 13, 245–259.
- 733 36. Kendall, M. G. 1975: Rank correlation methods. Charles Griffin. London, p. 202.
- 734 37. Jong, S. I., K. C. Om, and Y. I. Pak, 2021: Influences of atmospheric circulation patterns on  
 735 interannual variability of winter precipitation over the northern part of the Korean Peninsula.  
 736 *Clim. Res.*, 85, 35–50.
- 737 38. Mokhtarzad M., M., F. Eskandari, N. J. Vanjani, and A. Arabasadi, 2017: Drought forecasting  
 738 by ANN, ANFIS, and SVM and comparison of the models. *Environ. Earth Sci.*, 76, 729.  
 739 doi:10.1007/s12665-017-7064-0.
- 740 39. Wilks, D.S., 1995: Statistical methods in the atmospheric sciences: an introduction. Academic  
 741 Press, San Diego, CA.
- 742 40. Gong, D.-Y., J. Yang, D. Guo, M. Hu, S.-J. Kim, Y. Gao, D. Guo, T. Zhou, and M. Hu. 2011:  
 743 Spring Arctic Oscillation–East Asian Summer Monsoon Connection through Circulation  
 744 Changes over the Western North Pacific. *Climate Dynamics* 41:3085–3096.
- 745 41. Shen, B. Z., Z. D. Lin, R.Y. Lu, and Y. Lian, 2011: Circulation anomalies associated with  
 746 interannual variation of early-and late-summer precipitation in Northeast China. *Sci. Chin.  
 747 Earth Sci.*, 54, 1095–1104.
- 748 42. Wu, B., and J. Wang, 2002: Winter Arctic Oscillation, Siberian High and East Asian winter  
 749 monsoon. *Geophysical Research Letters*, 29(19), 1897. <https://doi.org/10.1029/2002GL015373>
- 750 43. Koster, R. D., et al., 2004: Regions of strong coupling between soil moisture and precipitation.  
 751 *Science*, 305(5687), 1138–1140.
- 752 44. Lorenz, E. N., 1963: Deterministic nonperiodic flow. *J. Atmos. Sci.*, 20, 130–141.  
 753 [https://doi.org/10.1175/1520-0469\(1963\)020<0130:DNF>2.0.CO;2](https://doi.org/10.1175/1520-0469(1963)020<0130:DNF>2.0.CO;2)
- 754 45. Wilks, D.S., 2011: Statistical Methods in the Atmospheric Sciences. 3rd ed. Academic Press,



755 Amsterdam, 100 pp.

756 46. WMO, 2012: Standardized Verification System (SVS) for Long-Range Forecasts (LRF).  
View Article Online  
DOI: 10.1039/C2EM0029K

757 WMO-No. 1091, World Meteorological Organization, Geneva, 47 pp.

758 47. Yu, T., Chen, W., Huang, P., Huang, G., & Yang, X., 2025: Weakened influence of ENSO on  
759 the East Asian summer monsoon since the early 2000s. *npj Climate and Atmospheric Science*,  
760 8(114), <https://doi.org/10.1038/s41612-025-00983-4>.

761

762



## Data availability statement

View Article Online  
DOI: 10.1039/D6EA00029K

Data are available from the corresponding author upon request.

